

Diamond NV center quantum magnetic sensor using a dual-frequency broadband antenna

Ke-Qi Shi(施柯琦), Heng Hang(杭衡), Wen-Tao Lu(卢文韬), Jing-Cheng Huang(黄竟成), Na Li(李娜), Jin-Xu Wang(王金旭), Zeng-Bo Xu(许增博), Yu-Lin Yan(虞林嫣), Sheng-Kai Xia(夏圣开), Yu-Chen Bian(卞雨辰), and Guan-Xiang Du(杜关祥)

Citation: Chin. Phys. B, 2025, 34 (**9**): 094205. DOI: 10.1088/1674-1056/add900
http://cpb.iphy.ac.cn; http://iopscience.iop.org/cpb

What follows is a list of articles you may be interested in

Optical PAM-4/PAM-8 generation via dual-Raman process in Rydberg atoms

Xiao-Yun Song(宋晓云), Zheng Yin(尹政), Guan-Yu Ren(任冠宇), Ming-Zhi Han(韩明志), Ai-Hong Yang(杨艾红), Yi-Hong Qi(祁义红), and Yan-Dong Peng(彭延东)

Chin. Phys. B, 2024, 33 (**6**): 064203. DOI: 10.1088/1674-1056/ad3344

Frequency-tunable single-photon router based on a microresonator containing a driven three-level emitter

Jin-Song Huang(黄劲松), Jing-Lan Hu(胡菁兰), Yan-Ling Li(李艳玲), and Zhong-Hui Xu(徐中辉)

Chin. Phys. B, 2024, 33 (**6**): 064202. DOI: 10.1088/1674-1056/ad362a

Design of compact integrated diamond nitrogen-vacancy center quantum probe

Sheng-Kai Xia(夏圣开), Wen-Tao Lu(卢文韬), Xu-Tong Zhao(赵旭彤), Ya-Wen Xue(薛雅文), Zeng-Bo Xu(许增博), Shi-Yu Ge(葛仕宇), Yang Wang(汪洋), Lin-Yan Yu(虞林嫣), Yu-Chen Bian(卞雨辰), Si-Han An(安思瀚), Bo Yang(杨博), Jian-Jun Xiang(向建军), and Guan-Xiang Du(杜关祥)

Chin. Phys. B, 2024, 33 (**5**): 054202. DOI: 10.1088/1674-1056/ad2bf6

Versatile and controlled quantum teleportation network

Yao-Yao Zhou(周瑶瑶), Peng-Xian Mei(梅鹏娴), Yan-Hong Liu(刘艳红), Liang Wu(吴量), Yan-Xiang Li(李雁翔), Zhi-Hui Yan(闫智辉), and Xiao-Jun Jia(贾晓军)

Chin. Phys. B, 2024, 33 (**3**): 034209. DOI: 10.1088/1674-1056/ad1981

Light slowing and all-optical time division multiplexing of hybrid four-wave mixing signal in nitrogen-vacancy center

Ruimin Wang(王瑞敏), Irfan Ahmed, Faizan Raza, Changbiao Li(李昌彪), Yanpeng Zhang(张彦鹏)

Chin. Phys. B, 2020, 29 (**5**): 054204. DOI: 10.1088/1674-1056/ab7b50

Diamond NV center quantum magnetic sensor using a dual-frequency broadband antenna

Ke-Qi Shi(施柯琦)[1], Heng Hang(杭衡)[1], Wen-Tao Lu(卢文韬)[2], Jing-Cheng Huang(黄竟成)[1], Na Li(李娜)[1], Jin-Xu Wang(王金旭)[1], Zeng-Bo Xu(许增博)[4], Lin-Yan Yu(虞林嫣)[1], Sheng-Kai Xia(夏圣开)[3], Yu-Chen Bian(卞雨辰)[2], and Guan-Xiang Du(杜关祥)[1,†]

[1] *College of Telecommunications and Information Engineering, Nanjing University of Posts and Telecommunications, Nanjing* 210003, *China*
[2] *Portland Institute, Nanjing University of Posts and Telecommunications, Nanjing* 210023, *China*
[3] *School of Computer Science and Technology, Nanjing University of Posts and Telecommunications, Nanjing* 210023, *China*
[4] *School of Economics, Nanjing University of Posts and Telecommunications, Nanjing* 210023, *China*

(Received 12 February 2025; revised manuscript received 12 April 2025; accepted manuscript online 15 May 2025)

This paper presents a compact broadband antenna that overcomes bandwidth limitations in a diamond nitrogen-vacancy (NV) center-based quantum magnetic sensor. Conventional antennas struggle to achieve both broadband operation and compact integration, restricting the sensitivity and dynamic range of the sensor. The broadband antenna based on a dual-frequency monopole structure achieves a bandwidth extension of 777 MHz at the Zeeman splitting frequency of 2.87 GHz, with the dual resonant points positioned near 2.87 GHz. Additionally, high-resolution imaging of the microwave magnetic field on the antenna surface was performed using a diamond optical fiber probe, which verified the dual-frequency design principle. Experimental results using the proposed antenna demonstrate the outstanding performance of the NV center-based magnetic sensor: a sensitivity of 55 nT/Hz$^{1/2}$ and a dynamic range of up to 54.0 dB. Compared to sensors using conventional antennas, the performance has been significantly improved.

Keywords: nitrogen-vacancy center, broadband antenna, quantum magnetometry, dual-frequency structure

PACS: 42.50.Ex, 07.55.Ge, 03.65.Yz

DOI: 10.1088/1674-1056/add900 **CSTR:** 32038.14.CPB.add900

1. Introduction

With the advancement of modern quantum technology, quantum computing, quantum communication, and quantum precision measurement all rely on qubits, a novel computing paradigm distinct from classical bits.[1–3] The diamond nitrogen-vacancy (NV) center possesses a unique electronic energy level structure and, owing to its exceptional optical properties and strong coherence, has been highly acclaimed and widely recognized in both the physics and engineering communities as an outstanding qubit carrier.[4,5]

In the fields of quantum computing, quantum communication, and quantum precision measurement, the mainstream technological route for the diamond NV center involves the initialization, manipulation, and readout of spin states.[6,7] Among these, microwave manipulation techniques include optically detected magnetic resonance (ODMR),[8] electron spin resonance (ESR),[9] Rabi oscillations,[10] and spin echo techniques.[11] In sensor applications, the antenna's magnetic field must resonate with the NV center's energy transitions to precisely manipulate its atomic-scale electron spins and quantum states.

Currently, microwave resonators, patch antennas, coplanar waveguides (CPW), and copper wires are commonly used for the microwave transmission and radiation components of sensing systems.[12–14] In 2014, Bayat, *et al*. proposed a structure of a double split-ring resonator,[15] with a resonant frequency close to 2.87 GHz at room temperature. However, due to its narrow bandwidth, it can only handle ODMR spectra measurements with a single resonant peak, making it difficult to observe multiple resonances in the range of 10 MHz–100 MHz under weak external magnetic fields. Additionally, changes in the external magnetic field can cause a mismatch between the resonant frequencies of the microwave source and the NV center. This mismatch can decrease power applied to the NV center by the microwave source, reducing fluorescence contrast and sensitivity. In severe cases, the sensor may be unable to detect the fluorescence signal radiated by the NV center.[16] In 2017, Polina Kapitanova *et al*. proposed a dielectric resonator antenna (DRA) consisting of the hollow cylinder dielectric resonator excited by a symmetric microstrip loop,[17] which can provide a uniform three-dimensional (3D) microwave field for spin manipulation of ensembles of the NV center in bulk diamond. However, with the development of modern sensing technologies, a tapered fiber diamond probe has been introduced. Compared to bulk diamonds, these probes do not need direct contact with RF equipment and can match smaller diamond samples (down to micron sizes), en-

†Corresponding author. E-mail: duguanxiang@njupt.edu.cn

© 2025 Chinese Physical Society and IOP Publishing Ltd. All rights, including for text and data mining, AI training, and similar technologies, are reserved.

hancing spatial resolution in measurements while minimizing interference with RF devices.[18]

In this paper, we designed a dual-frequency broadband antenna (DBA) suitable for quantum magnetic sensors based on micron-sized NV center samples using Ansys HFSS 19.1. Our work is developed through the following points:

(i) Design a broadband antenna based on a dual-frequency monopole structure, where the dual resonant points are close to the Zeeman splitting frequency of 2.87 GHz, to achieve a bandwidth extension of 777 MHz.

(ii) Employ an optical fiber diamond probe to perform high-resolution imaging of the microwave magnetic fields on the antenna surface at frequencies of 2.75 GHz (low frequency), 2.87 GHz (the zero-field splitting value of NV center), and 2.98 GHz (high frequency), to verify the design principle of dual-frequency points with extended bandwidth.

(iii) Apply DBA as a microwave source for NV center-based magnetic sensor, and conduct ODMR experiments to determine that the maximum detectable magnetic field strength is 1.39 $\times 10^{-2}$ T. Under these conditions, the sensitivity of the magnetic sensor is 55 nT/Hz$^{1/2}$, and the detected dynamic range reaches up to 54.0 dB.

2. Basic theory and experimental setup

When a nitrogen atom replaces a carbon atom in the diamond crystal structure, and an adjacent C atom is missing, creating a vacancy that traps an electron, we call this type of defect structure an NV structure,[19] as shown in Fig. 1(a). The NV center in diamond exhibits C_{3V} symmetry, with their symmetry axes (NV axes) having four distinct and fixed crystallographic orientations, designated as NV$_\alpha$, NV$_\beta$, NV$_\gamma$, and NV$_\delta$. The NV center we studied is the NV$^-$ center, which contains 6 electrons in 4 orbitals. Each orbital can hold two electrons with opposite spins, resulting in a total of eight different electron states. Through optically detected magnetic resonance (ODMR) experiments, these eight different electron states can be easily observed. Among the six electrons, two pairs are paired up, leaving two unpaired electrons due to spin–spin coupling, forming a spin triplet (with spin $S = 1$) in the ground and excited states, with spin levels of $m_s = 0$ and $m_s = \pm 1$, forming two quantum two-level systems.[20]

The energy level structure of the diamond NV center is shown in Fig. 1(b). Due to the presence of electron spin and nuclear spin, the NV center has a complex energy level structure, including the triplet ground state (^{3}A$_2$), the triplet excited state (^{3}E), and the metastable state (^{1}E).

When there is no external magnetic field, the NV center is in its ground state triplet, with the $m_s = 0$ state and the degenerate doublet states with $m_s = \pm 1$, separated by a zero-field splitting of 2.87 GHz. The energy difference between $m_s = 0$ and $m_s = \pm 1$ arises from the interaction between electron spins within the NV center, a phenomenon known as zero-field splitting (ZFS). At room temperature, the energy level difference caused by this splitting corresponds to a frequency of 2.87 GHz, which is determined by the crystal structure of the NV center and is independent of the external magnetic field. The zero-field splitting frequency serves as a critical benchmark for microwave-driven spin manipulation, enabling precise control of the quantum states of the NV center. When an external magnetic field is applied, the degenerate doublet states with $m_s = \pm 1$ will undergo a Zeeman splitting into two sublevels with $m_s = +1$ and $m_s = -1$. The Hamiltonian of the NV center under the influence of an external static magnetic field can be written as the following formula:[21]

$$H = DS_z^2 + E\left(S_x^2 - S_y^2\right) + \gamma \cdot \boldsymbol{B} \cdot \boldsymbol{S}, \tag{1}$$

where $D = 2.87$ GHz is the zero-field splitting value of the ground state at room temperature, $\boldsymbol{S} = \{S_x, S_y, S_z\}$ is the spin matrix of the electron, E is the horizontal zero-field splitting coefficient representing the electric field strength, γ is the electron gyromagnetic ratio of the NV center, with a value of 28 GHz/T, and B represents the magnitude of the static magnetic field.

Using optical detection of magnetic resonance (ODMR), we can probe the transitions from $m_s = 0$ to $m_s = +1$ and $m_s = -1$, and measure the resonance frequencies $f_{i\pm}$ corresponding to the four axes of the NV center, where i represents the four axes of the NV center. These appear as eight peaks on the ODMR spectrum. For a given axis, the strength of the external magnetic field and the resonance frequencies can be obtained from[22]

$$B_i = \left(f_{i+} - f_{i-}\right)/2\gamma. \tag{2}$$

Figure 1(c) is a schematic diagram of the experimental system, which consists of three main modules: the optical module, the microwave pumping module, and the scanning module.[23]

The optical module primarily integrates a laser generator, a mirror, a dichroic mirror, objectives, and an avalanche photodiode (APD) for laser pumping and fluorescence signal collection. A 532-nm laser with adjustable and continuous emission power is selected for generating green lasers and focused onto the fiber-optic quantum probe via the objective. This excites the NV center, which emits 637-nm red fluorescence during its transition back to the ground state. The APD collects this fluorescence and converts the optical signal into an electrical signal. The microwave pumping module consists of an arbitrary sequence generator, a microwave source, an RF microwave switch, and a power amplifier. By configuring three output pulse signals, precise microwave signal control is achieved, enabling the manipulation of the quantum state of the diamond

NV center. The scanning module is divided into scanning and software-controlled imaging sections. The scanning section utilizes a motorized displacement stage and a tapered fiber diamond probe. By controlling the step diameter of the displacement stage, the device under the test is scanned point by point, and a two-dimensional (2D) array of fluorescence signal data is obtained to create the microwave field imaging of the device under the test. The software-controlled imaging section employs a LabVIEW program to configure experimental parameters, facilitating data processing, display, and storage.

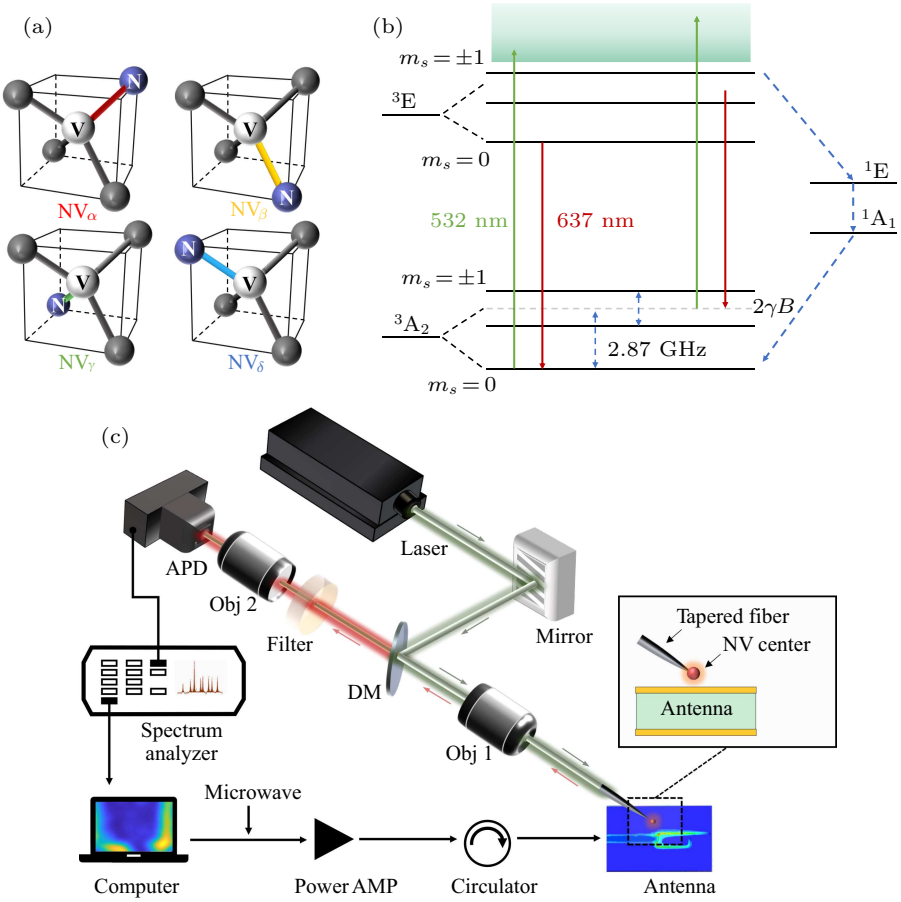


Fig. 1. (a) Diamond NV center structure, (b) diamond NV center energy level diagram, (c) schematic diagram of the experimental setup.

3. Dual-frequency broadband antenna design

The zero-field splitting frequency (2.87 GHz) of the NV center serves as the reference frequency for microwave-driven spin transitions. However, under an external magnetic field, the resonance frequencies of the $m_s = \pm 1$ states shift due to the Zeeman effect. To accommodate such shifts, the antenna must provide a broadband response centered at 2.87 GHz, ensuring its frequency range covers the intrinsic zero-field splitting frequency and the shifted frequencies induced by the magnetic field. This enables stable quantum state manipulation across a wide dynamic range. To achieve this, we have incorporated a dual-frequency resonance mechanism into the antenna design, ensuring that both resonance frequencies are closely centered around 2.87 GHz, thereby significantly enhancing the operational bandwidth. Unlike conventional dual-band designs that merely combine two isolated frequency bands,[24] our dual-frequency antenna achieves continuous broadband response through precisely engineered coupling between asymmetric monopole arms, representing an innovative application of dual-band antenna technology. Figure 2 shows the overall structure of the antenna, which consists of five parts: substrate, high frequency (2.9 GHz) monopole antenna, low frequency (2.8 GHz) monopole antenna, microstrip feedline, and reference ground.

The antenna is based on the design of a dual-frequency monopole antenna, which is an antenna that can operate in two different frequency bands.[24] This is achieved by adjusting the physical size and structure of the antenna to resonate at two specific frequencies. The short and long arms on the left and right sides of the antenna's front patch correspond to the high and low frequencies of the dual-band system. The lengths of the long and short arms can be calculated as 1/4 wavelength monopole antenna according to Eqs. (3) and (4).

When propagation in free space:

$$L_m = c/4f. \tag{3}$$

When propagation in a medium:

$$L_{m_\mathrm{sub}} = c/4f\sqrt{\varepsilon_\mathrm{e}}, \tag{4}$$

where c is the speed of light in a vacuum, and ε_e is the effective dielectric constant, determined by the following Eq. (5) (when $W_l > h$).

$$\varepsilon_e = \frac{\varepsilon_r + 1}{2} + \frac{\varepsilon_r - 1}{2}\left(1 + 12\frac{h}{W_l}\right)^{-1/2}, \tag{5}$$

where ε_r is the dielectric constant, h is the thickness of the substrate, and W_l is the width of the feedline.

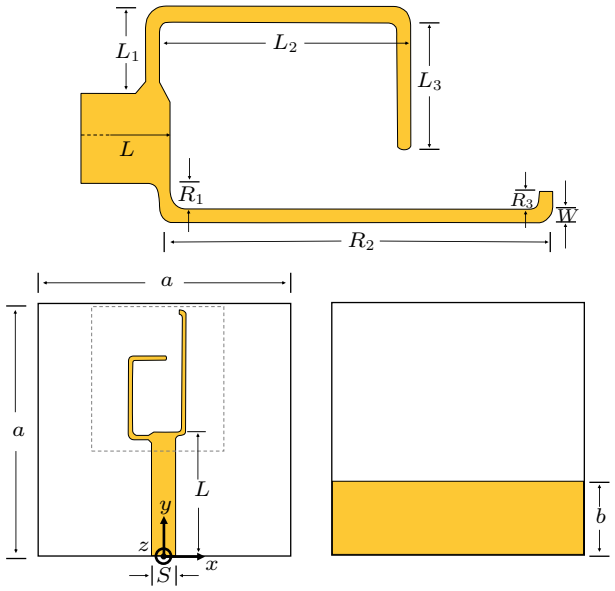


Fig. 2. Schematic diagram of antenna design parameters.

As shown in Fig. 2, the antenna uses the cost-effective and widely available F4BM220 substrate, which has a relative permittivity ε_r of 2.2, a loss tangent $\tan\delta$ of 0.001, and a substrate thickness h of 1.5 mm. The stable dielectric constant of the substrate ensures minimal frequency drift under temperature fluctuations. Additionally, the low-loss tangent reduces energy loss during signal transmission, thereby minimizing the impact of external electromagnetic interference on the antenna's performance.[25] According to Eqs. (3)–(5), for the high-frequency band with a center frequency of 2.9 GHz, if the wave transmits in free space, the length of the 1/4 wavelength monopole antenna is 25.9 mm; if it transmits in a medium, the length is 17.9 mm. Similarly, for the low-frequency band with a center frequency of 2.8 GHz, the antenna length is 26.8 mm in free space and 18.5 mm in a medium. For a microstrip monopole antenna on a PCB, the wave transmission must pass through both the substrate and free space, so the actual wavelength should fall between the two. Therefore, for the 2.9-GHz resonant frequency, the antenna size should range from 17.9 mm to 25.9 mm; for the 2.8-GHz resonant frequency, it should range from 18.5 mm to 26.8 mm. These are the calculated initial size ranges for the two 1/4 wavelength monopole antennas. However, in practical simulations, even though the size range is known, continuous adjustment and optimization are required to determine the final dimensions. The optimized antenna sizes are shown in Table 1.

Table 1. Main parameters of the dual-frequency broadband antenna.

Parameter	Description	Value (mm)
t_{Cu}	patch thickness	0.018
S	the width of the microstrip feeder	3.5
L	the length of the microstrip feeder	19
W	The width of the metal sheet of the monopole antenna	0.5
a	the length and width of the PCB	38
b	the width of the GND	11
r_{cut}	the radius of the fillet at the corners of the patch	0.85
L_1	the length of the first segment of the high-frequency monopole antenna	3.5
L_2	the length of the second segment of the high-frequency monopole antenna	12
L_3	the length of the third segment of the high-frequency monopole antenna	5
R_1	the length of the first segment of the low-frequency monopole antenna	1
R_2	the length of the second segment of the low-frequency monopole antenna	19
R_3	the length of the third segment of the low-frequency monopole antenna	0.5

4. Antenna characterization experiment

4.1. Measure the S_{11} parameters of the antenna

The S parameter is an important index representing the transmission performance of the antenna, and the S_{11} parameter is defined as the reflection coefficient of the input end of the antenna, which is the ratio of the reflected power and the incident power between the signal source and the antenna. Figure 3(a) shows the DBA after processing. Microwave power is input from the SMA connector on the left. Connect the antenna to a vector network analyzer (Ceyear-3672D, 10 MHz–50 GHz) to measure S_{11} and record data. Figure 3(b) shows the collected data; the blue line is the simulation data from Ansys HFSS 19.1, and the red line is the data measured by the vector network analyzer. When the frequency range is set to 2.1 GHz–3.5 GHz, the simulation results show a good agreement with the experimental data. The bandwidth obtained by simulation is approximately 880 MHz, while the bandwidth obtained by experimental measurements is approx-

imately 777 MHz. The deviation between the simulation and experimental measurement is caused by the mismatch between the laboratory interface and the antenna interface, so the measured data is S_{11} combined with the antenna and interface. At the same time, due to uncertainties such as the material of the PCB and the processing error (the line error of ± 0.02 mm), the actual measurement of S_{11} will also lead to deviations from the simulation. It can be seen from the measurement results that the minimum value of S_{11} is -36.395 dB, indicating that the antenna has achieved good matching impedance and low return loss.

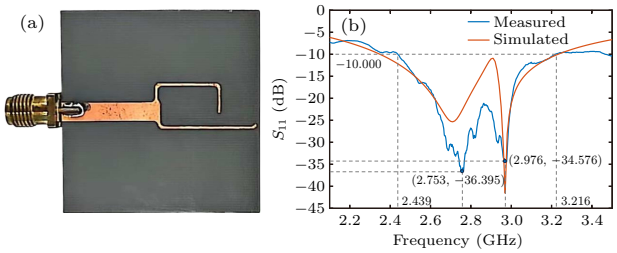


Fig. 3. (a) The dual-frequency broadband antenna on a PCB and (b) simulation data and measurement data of S_{11}.

4.2. Magnetic imaging of the antenna surface

High-resolution imaging of microwave magnetic fields has been primarily constrained by the size of the NV center and the distance between the NV center and the device under test. We employed a fiber diamond probe to achieve high-resolution imaging of the microwave magnetic field distribution on the antenna surface. As detailed in Fig. 5(a), the selected NV center size was 6 μm, and the vertical distance between the NV center and the antenna was 30 μm.[26] While bulk diamond configurations eliminate the need for electric displacement stages and point-by-point scanning, they require direct contact with the antenna, which may perturb the target microwave field and degrade antenna transmission performance.[18] Therefore, to enable precise microwave magnetic field mapping while preserving the antenna's transmission characteristics, we adopted the fiber-integrated diamond probe architecture.

We started with optical detection magnetic resonance experiments to achieve magnetic imaging of the microwave antenna surface. Before initiating the ODMR experiment, we first applied an external modulation method to the microwave signal fed into the device, using quantum state pulse sideband modulation. The microwave pulse acted on the NV center, converting the measurement of the fluorescence main frequency signal into the measurement of the fluorescence sideband signal, thereby achieving high signal-to-noise ratio measurements.[27]

Under an external magnetic field, the diamond NV center undergoes Zeeman splitting, which appears in the ODMR spectrum as an increased separation between resonance peaks, meaning a single peak splits into multiple peaks. Due to the four possible NV axes, each with distinct spin-state transitions, the ODMR spectrum displays a total of eight non-overlapping peaks.[23] By adjusting the relative position of the permanent magnet and the diamond sample, an ODMR spectrum with eight well-separated peaks can be obtained. To analyze the data, we fitted the raw data points using a Lorentzian function and represented them as

$$S(A, w, f_0) = \frac{Aw^2}{(f - f_0)^2 + w^2}, \tag{6}$$

where S is the actual detected fluorescence intensity signal, A is the maximum fluorescence intensity signal of each spectral peak, $2w$ is the full width at half maximum, f is the frequency of the microwave, and f_0 is the center frequency of the resonant peak.

Figure 4(a) shows the ODMR spectrum obtained after applying a static magnetic field with the microwave antenna, and eight distinct spectral peaks can be observed, and also defines the NV axis corresponding to four pairs of symmetrical resonance peaks respectively as NV symmetry axis-α, axis-β, axis-γ, and axis-δ. The blue data points in the figure represent the actual measured data, while the red curve is the fitted curve using a Lorentzian function.

After performing the ODMR experiment, we continued with the Rabi oscillation experiment on the surface of the DBA. The Rabi oscillation frequency was set to 2.77 GHz, corresponding to one of the peak frequencies observed in the ODMR spectrum. At this frequency point, dual pumping was applied to the diamond NV center, and the pulse microwave interaction time was varied. The measured fluorescence signal was then plotted as the vertical axis, with the microwave interaction time as the horizontal axis, allowing us to obtain the Rabi oscillation curve, which was subsequently fitted using[27]

$$S(B_{\mathrm{mw}}, \tau) = I_0 - i_0 \sin(2\pi\gamma B_{\mathrm{mw}} t) \cdot \mathrm{e}^{-t/\tau}, \tag{7}$$

where S represents the actual detected fluorescence amplitude, B_{mw} is the intensity of the microwave magnetic field, t is the microwave excitation duration, τ is the decay time of the Rabi oscillation, I_0 is the fluorescence intensity of the NV center polarized to the ground state $m_s = 0$, i_0 is the amplitude of the Rabi oscillation, and γ is the gyromagnetic ratio of the NV center electron spin.

By scanning each position of the antenna, complete Rabi oscillations can be obtained to determine the local microwave field strength. However, this process is extremely time-consuming. Therefore, instead of executing a full Rabi sequence to extract the oscillation frequency at each position, we employ a pulsed Rabi sequence with a fixed and relatively short microwave pulse duration. When the microwave excitation duration t is short ($t \ll \tau$), $2\pi\gamma B_{\mathrm{mw}} t$ in Eq. (7) approaches 0. According to the properties of the sine function, at this point, $\sin(2\pi\gamma B_{\mathrm{mw}} t)$ is approximately equal to $2\pi\gamma B_{\mathrm{mw}} t$, and the term $\mathrm{e}^{-t/\tau}$ approaches 1. Therefore, the Rabi oscillation

curve can be considered a direct proportional function and simplified to the following equation:

$$S(B_{\mathrm{mw}}, \tau) = I_0 - 2\pi\gamma B_{\mathrm{mw}} t \cdot i_0. \tag{8}$$

We performed data fitting of the actual measurement points using Matlab, with the results shown in Fig. 4(b). The blue data points represent the measured values, while the red curve shows the fitted results. At $t = 200$ ns (blue dashed line), the amplitude increases significantly with the microwave excitation duration, and the red fitting curve exhibits no oscillation characteristics, conforming to a linear response.[27] Furthermore, based on the fitting results, we obtained a Rabi oscillation decay time $\tau = 636$ ns with the decoherence attenuation factor $e^{-t/\tau}$ (~ 0.73) approaching 1 at this stage. At the same time, according to Eq. (9), the microwave magnetic field B_{mw} of the device under test is proportional to the Rabi oscillation frequency w.

$$B_{\mathrm{mw}} = \frac{w}{\gamma}. \tag{9}$$

According to Eqs. (7)–(9), when the microwave excitation duration t is very short, the fluorescence intensity is proportional to the magnetic field strength. Therefore, in the magnetic imaging experiment, we set the microwave duration to 200 ns to ensure that the fluorescence intensity changes linearly with the magnetic field strength, thereby enabling faster and more efficient microwave magnetic field imaging.

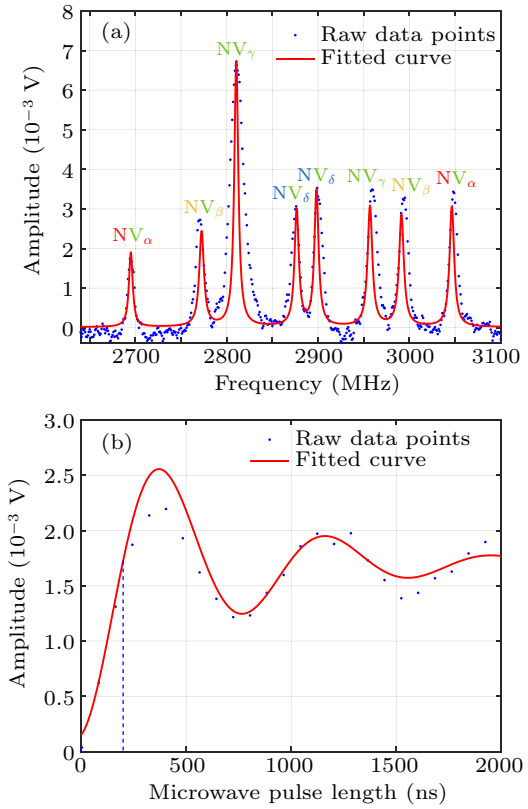


Fig. 4. (a) The ODMR spectrum of the NV center is under the influence of a static magnetic field. (b) Measurement data and fitted curve of a typical Rabi oscillation at a microwave frequency of 2.77 GHz.

The magnetic field simulation shows weaker field strength at the ends of the long and short arms compared to the region near the microstrip line, making the latter ideal for verifying their relative strengths. To enhance measurement accuracy, we defined the dashed box in Fig. 5(b) as the desired imaging area (DIA) of the magnetic field, with both the length and width of the scanning area set to 9100 μm. In Ansys HFSS 19.1 software, the data point interval was set to 200 μm, and figure 5(c) presents the simulated surface magnetic field distribution of the microwave antenna at the resonance frequency of 2.87 GHz. The data are normalized for visualization and analysis. To obtain a more accurate characterization of the microwave magnetic field distribution on the antenna surface, an LabVIEW program was used for precise control to scan the DIA region. Figure 5(d) shows the measurement results of the distribution characterization on the surface of the microwave antenna corresponding to the frequency 2.87 GHz at a microwave power of 30 dBm. The comparison of Figs. 5(c) and 5(d) indicates that the experimental findings are in good agreement with the simulation results.

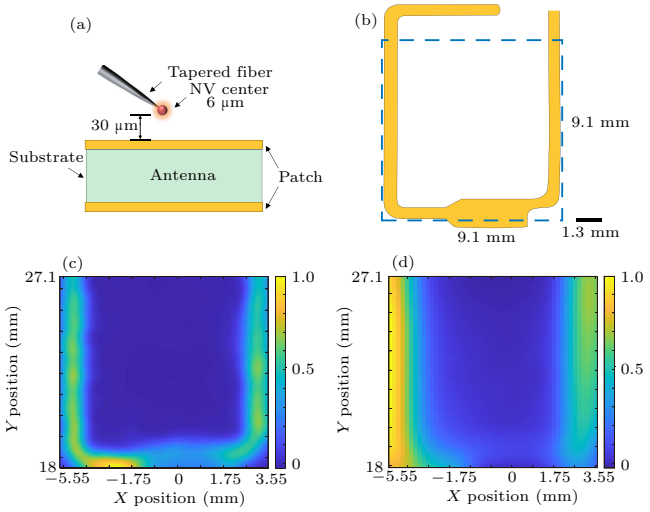


Fig. 5. (a) Schematic diagram of the antenna and fiber diamond probe placement. (b) The area inside the blue dashed box is the area to be imaged. (c) Simulation result of the microwave magnetic field distribution on the antenna surface at the Zeeman splitting frequency of 2.87 GHz. (d) Experimental scanning result of the microwave magnetic field distribution on the antenna surface at 2.87 GHz (the zero-field splitting value of NV center).

After analyzing the microwave magnetic field distribution at the resonant frequency of 2.87 GHz, we further examined its distribution at 2.75 GHz and 2.98 GHz. Similarly, figures 6(a) and 6(c) show the surface magnetic field distribution diagram of the microwave antenna obtained by simulation at the frequency of 2.75 GHz and 2.98 GHz, respectively. Figures 6(b) and 6(d) show the experimental results of the distribution characteristics of the microwave antenna surface at the frequencies of 2.75 GHz and 2.98 GHz. Figures 6(a) and 6(c) present the simulated surface magnetic field distributions at the frequencies of 2.75 GHz and 2.98 GHz, while figures 6(b) and 6(d) show the corresponding experimental results. The

comparisons demonstrate strong agreement between simulation and experiment, validating the design principle of our DBA. Specifically, at 2.98 GHz, the short arm plays a dominant role, as indicated by its relatively higher magnetic field intensity compared to the long arm. Conversely, at 2.75 GHz, the long arm is the primary working component. By bringing the high-frequency and low-frequency points closer together to enhance the bandwidth, the magnetic field intensities of the long and short arms become comparable at the desired resonance frequency of 2.87 GHz, as shown in Fig. 5(c). This indicates that at 2.87 GHz, both the long and short arms contribute to the operation.

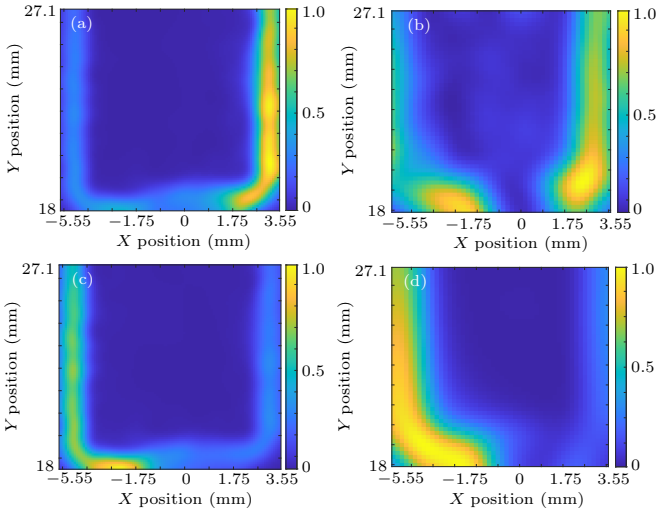


Fig. 6. (a) Simulation result of the microwave magnetic field distribution on the antenna surface at 2.75 GHz (low frequency). (b) Experimental scanning result of the microwave magnetic field distribution on the antenna surface at 2.75 GHz. (c) Simulation result of the microwave magnetic field distribution on the antenna surface at 2.98 GHz (high frequency). (d) Experimental scanning result of the microwave magnetic field distribution on the antenna surface at 2.98 GHz.

4.3. Application of dual-frequency broadband antenna in NV center-based magnetic sensor

The NV center is widely used for nanoscale magnetic field measurements due to its sensitivity to magnetic fields via its electron spin. The $m_s = \pm 1$ state of the ground state energy level of the NV center undergoes energy level splitting due to the Zeeman effect in a magnetic field, and the energy level difference caused by the splitting is proportional to the magnetic field strength. Furthermore, as described by Eq. (2), when an external magnetic field of varying intensity is applied, the energy level splitting of the NV center causes its resonance frequency to shift accordingly.

As a critical component of NV center-based magnetic sensors, the antenna is responsible for delivering microwave signals and continuously pumping the NV center during the low-level phase of the pulsed laser to manipulate its quantum state. The bandwidth of the antenna determines the range of microwave frequencies it can provide, thereby affecting the resonance frequency coverage of the NV center. A broadband antenna can deliver a continuous and wide frequency range, effectively covering the resonance frequency shifts caused by Zeeman splitting under varying external magnetic fields. This ensures that an appropriate matching frequency can always be found, enabling strong magnetic field characterization based on the NV center while enhancing the sensitivity and dynamic range of the sensors.

The sensitivity of the antenna for measuring the magnetic field is equal to the measured noise spectral density (NSD, in units of V/Hz$^{1/2}$) divided by the sensor responsivity (in units of V/T). The sensor responsivity is equal to the microwave frequency responsivity m (in units of V/MHz) multiplied by the electron gyromagnetic ratio γ (with a value of 28 GHz/T), where the sensor responsivity represents the conversion relationship between fluorescence intensity and magnetic field. This can be expressed by the following equation:[28]

$$\eta = \frac{\mathrm{NSD}}{\gamma m}. \tag{10}$$

The noise floor in the experiment is measured by monitoring the NSD read from the sensor. By simultaneously scanning the modulation frequency and monitoring the noise readings from the lock-in amplifier, the output voltage noise spectral density is measured to be $\sim 2.27 \times 10^{-7}$ V/Hz$^{1/2}$.[28] Meanwhile, the antenna designed in this paper and the diamond NV center sample are placed in a controllable magnetic field. A pulse generator produces laser and microwave modulation pulses, with the reference frequency of the phase-locked amplifier set to the external reference, a cutoff frequency of 1 Hz, and demodulating the APD output signal. By differentiating the data near the zero point of the ODMR resonance curve, the absolute value of the microwave frequency responsivity $|m|$ is calculated to be 1.4623×10^{-4} V/MHz.[28] From this, the sensitivity of the magnetic sensor using DBA as the microwave source was estimated to be 55 nT/Hz$^{1/2}$. The dynamic range of the sensor can be determined by the ratio of the maximum detectable magnetic field to the minimum detectable magnetic field, which is defined as the ratio of the bandwidth divided by the value of twice the gyromagnetic ratio to the sensitivity. Table 2 presents a comparative analysis of NV center-based magnetic sensors in the existing literature, focusing on designs that employ different types of antennas as microwave sources. Compared to the resonator,[15] broadband patch antenna,[29] and filtering antenna,[30] the sensor using DBA as the microwave source demonstrates significant performance improvements, achieving a sensitivity of 55 nT/Hz$^{1/2}$ and a maximum dynamic monitoring range of 54.0 dB.

To further verify the superiority of the DBA as a microwave source for NV center-based magnetic sensors, we conducted additional performance tests on both the CPW and flexible antenna under identical experimental conditions. In the experiment, the diamond sample of the CPW is located in the microwave uniform distribution area in the center of the waveguide, while the sample of the flexible antenna is located near the microwave's strongest point at the edge of the ring

hole.[31] Table 3 summarizes the key parameter comparisons among the DBA, CPW, and flexible antenna.

The results demonstrate that the DBA exhibits significantly higher sensitivity (55 nT/Hz$^{1/2}$) compared to the CPW (87.7 nT/Hz$^{1/2}$) and flexible antenna (83.1 nT/Hz$^{1/2}$), highlighting its superior competitiveness in high-precision magnetic field measurements. Furthermore, the dynamic range of the DBA (54.0 dB) shows an improvement of approximately 20% over the flexible antenna (44.8 dB), enabling detection across a broader range of magnetic field strengths. Although the CPW's bandwidth (0 GHz–50 GHz) far exceeds that of the DBA (0.777 GHz), the microwave responsivity of the DBA (1.4623×10^{-4} V/MHz) is 58% higher than that of the CPW (9.2464×10^{-5} V/MHz). This enhancement directly reflects the DBA's capability to efficiently couple microwave energy to the NV center, thereby improving fluorescence signal contrast and establishing a foundation for high-sensitivity magnetic sensing. In contrast, the DBA's dual-frequency structural design achieves an optimal balance between responsivity and dynamic range within its limited bandwidth, making it better suited for quantum sensing applications involving the NV center. When integrated with the literature data from Table 2 and the experimental comparisons in Table 3, the DBA demonstrates comprehensive performance advantages in sensitivity, dynamic range, and energy coupling efficiency, conclusively validating its superiority as a microwave source for quantum magnetic sensors.

Table 2. The comparison of NV center-based magnetic sensors in existing literature.

Ref.	Microwave delivery	Operating bandwidth (GHz)	Maximum detection range (T)	Sensitivity	Dynamic range (dB)
This	dual-frequency broadband antenna	0.777	1.39×10^{-2}	55 nT/Hz$^{1/2}$	54.0
[15]	split-ring resonator	0.04	5.59×10^{-4}	~fT/Hz$^{1/2}$	0.7
[29]	broadband antenna	2.64	9.43×10^{-2}	3.07 μT/Hz$^{1/2}$	44.9
[30]	open-loop ring filtering antenna	0.73	15.93×10^{-2}	8.52 μT/Hz$^{1/2}$	32.73

Table 3. The comparison of antenna performance under the same experimental conditions.

Parameter	This	CPW	Flexible antenna[31]
Microwave frequency responsivity	1.4623×10^{-4} V/MHz	9.2464×10^{-5} V/MHz	9.755×10^{-5} V/MHz
Sensitivity	55 nT/Hz$^{1/2}$	87.7 nT/Hz$^{1/2}$	83.1 nT/Hz$^{1/2}$
Dynamic range	54.0 dB	N/A	44.8 dB

5. Conclusion and perspective

In this study, we successfully designed a novel broadband antenna for NV center-based quantum magnetic field sensing. The dual-frequency broadband antenna (DBA) is suitable for submicron diamond NV center samples, enabling precise manipulation of quantum states. The antenna is based on a dual-frequency monopole structure design and achieves a bandwidth extension of 777 MHz around the zero-field splitting value of NV center (2.87 GHz). The simulation and experimental results are in excellent agreement, demonstrating that the antenna has good matching impedance and low return loss. We used an optical fiber scanning probe with NV center to probe the microwave magnetic field distribution on the antenna surface, validating the antenna's design concept of bandwidth extension through dual-frequency proximity. The experimental data obtained closely matched the simulation results. Compared with existing NV center-based magnetic sensor designs, the magnetic sensor employing DBA as the microwave source significantly improves magnetic field measurement sensitivity and dynamic range. This design provides critical support for precise magnetic field characterization techniques based on the diamond NV center while offering new perspectives for the development of future quantum magnetic sensors. Although the current configuration demonstrates excellent performance in laboratory settings, practical applications require further investigation into environmental factors affecting antenna performance. Additionally, the scalability of fabrication processes and feasibility of mass production demand thorough optimization. Future work will focus on enhancing the environmental robustness of the DBA and exploring cost-effective, large-scale manufacturing solutions to advance the practical implementation of quantum magnetic sensing technologies.

Acknowledgements

Project supported by the National Key Research and Development Program of China (Grant No. 2021YFB2012600), the Science and Technology Plan Project of the State Administration of Market Regulation, China (Grant No. 2021MK039), and the Suqian Talent Elite Program (Grant No. SQQN202414).

References

[1] O'Brien J L 2007 *Science* **318** 1567
[2] Gisin N and Thew R 2007 *Nat. Photon.* **1** 165
[3] Childs A M, Preskill J and Renes J 2000 *J. Mod. Opt.* **47** 155
[4] Batalov A, Jacques V, Kaiser F, Siyushev P, Neumann P, Rogers L J, McMurtrie R L, Manson N B, Jelezko F and Wrachtrup J 2009 *Phys. Rev. Lett.* **102** 195506
[5] Taylor J M, Cappellaro P, Childress L, Jiang L, Budker D, Hemmer P R, Yacoby A, Walsworth R and Lukin M D 2008 *Nat. Phys.* **4** 81
[6] Zheng D 2010 *Study and manipulation of photoluminescent NV color center in diamond* Ph.D. dissertation (Shanghai: East China Normal University)
[7] Savvin A, Dormidonov A, Smetanina E, Mitrokhin V, Lipatov E, Genin D, Potanin S, Yelisseyev A and Vins V 2021 *Nat. Commun.* **12** 7118
[8] Dmitriev A K and Vershovskii A K 2014 *J. Phys. Conf. Ser.* **541** 012090
[9] Bucher D B, Aude Craik D P L, Backlund M P, Turner M J, Ben Dor O, Glenn D R and Walsworth R L 2019 *Nat. Protoc.* **14** 2707
[10] Fuchs G D, Dobrovitski V V, Toyli D M, Heremans F J, Weis C D, Schenkel T and Awschalom D D 2010 *Nat. Phys.* **6** 668
[11] Maze J R, Stanwix P L, Hodges J S, Hong S, Taylor J M, Cappellaro P, Jiang L, Gurudev Dutt M V, Togan E, Zibrov A S, Yacoby A, Walsworth R L and Lukin M D 2008 *Nature* **455** 644
[12] Yang X, Zhang N, Yuan H, Bian G, Fan P and Li M 2019 *AIP Adv.* **9** 075213
[13] Jia W, Shi Z, Qin X, Rong X, Du J 2018 *Rev. Sci. Instrum.* **89** 064705
[14] Babashah H, Losero E and Galland C 2024 *Open Res. Eur.* **4** 44
[15] Bayat K, Choy J, Baroughi M F, Meesala S and Loncar M 2014 *Nano Lett.* **14** 1208
[16] Bürgler B, Sjolander T F, Brinza O, Tallaire A, Achard J and Maletinsky P 2023 *npj Quantum Inf.* **9** 56
[17] Kapitanova P, Soshenko V, Vorobyov V, Dobrykh D, Bolshedvorskiih S, Sorokin V and Akimov A 2017 *AIP Conf. Proc.* **1874** 030017
[18] Lu W T, Xi S K, Chen A Q, He K H, Xu Z B, Chen Y H, Wang Y, Ge S Y, An S H, Wu J F, Ma Y H and Du G X 2024 *Chin. Phys. B* **33** 080305
[19] Schirhagl R, Chang K, Loretz M and Degen C L 2014 *Annu. Rev. Phys. Chem.* **65** 1545
[20] Doherty M W, Dolde F, Fedder H, Jelezko F, Wrachtrup J, Manson N B and Hollenberg L C L 2012 *Phys. Rev. B* **85** 205203
[21] Adam Gali 2009 *Phys. Rev. B* **79** 235210
[22] Zhao X T, He F Y, Xue Y W, Ma W H, Yin X Z, Xia S K, Zeng M J and Du G X 2024 *Chin. Phys. B* **33** 048502
[23] Yang B, Dong M M, He W H, Liu Y, Feng C M, Wang Y J and Du G X 2019 *IEEE Trans. Microwave Theory Tech.* **67** 245
[24] Danuor P, Moon J I and Jung Y B 2023 *Sci. Rep.* **13** 9982
[25] Wei H R, He W H, Li Q Z, Yu Y Y, Xu R X, Zhou J, Shen J and Chen W 2023 *Ceram. Int.* **49** 28449
[26] Appel P, Ganzhorn M, Neu E and Maletinsky P 2015 *New J. Phys.* **17** 112001
[27] Dong M M, Hu Z Z, Liu Y, Yang B, Wang Y J and Du G X 2018 *Appl. Phys. Lett.* **113** 131105
[28] Ibrahim M I, Foy C, Englund D R and Han R 2021 *IEEE J. Solid-State Circuits* **56** 1001
[29] Cui M M, Shen F Z, Qiao Y Y, Du G X, Zhuo X, Zang J W, Zhang Z Y, Wang Y, Li L and Gao Y 2022 *Electron. Lett.* 58 893
[30] Gao Y, Zeng Y, Cui M M, Qiao Y Y, Yang X, Lin C N, Zhao J L, Li L, Wang Y and Shan C X 2022 *IEEE Trans. Instrum. Meas.* **71** 2005112
[31] Xia S K, Lu W T, Zhao X T, Xue Y, Xu Z B, Ge S Y, Wang Y, Yu L Y, Bian Y C, An S H, Yang B, Xiang J J and Du G X 2024 *Chin. Phys. B* **33** 054202